Response to Referee #1

We would like to thank the referee for their insightful comments and have responded below. The referee comments are highlighted in blue with our responses in black.
We have also included the revised manuscript with changes highlighted in red and blue.

General:
The manuscript reports lidar observations of optical properties of fresh fire smoke. Such observations are rare, if not absent in the literature. Usually, observations of aged smoke after long-range transport are presented in papers.
The paper is, to my opinion, very lengthy (section 3), like a review article on the methodology used. Section 4 is very interesting, but many figures are not needed when focusing on the Paris fire event. Minor revisions are required.

Details:
Abstract, L14-15: I would emphasize that you observed fresh smoke (only a few hours after emission).
We have added "fresh" for the description of the smoke, as:
"The first lidar measurement of a fresh smoke plume, emitted only a few hours after an accidental warehouse fire."

L17: The depolarization ratio is not only small when particles are spherical, also when they are very small, as shortly after fire emission events.
We agree, and we have changed this sentence to "suggesting the presence of either small particles or spherical hydrated aerosols in that layer".

P1, L28: I would use key words such as 'young smoke' and 'freshly emitted' in the introduction.
We made changes and used such descriptions now in the introduction, and also in the conclusion.

P4, L11, and Table 1: Is the initial signal resolution really 0.75m? Maybe 7.5m is correct!
Our initial resolution is really 0.75m, as we used a high-speed digitizer card with 200 MHz sampling frequency. This information is added in the text. But the final resolution after smoothing is 45 m.

Section 3, very lengths, nothing new in sections 3.1, 3.2, 3.3, 3.3.1, 3.3.2, 3.3.3. Do we need all this?
All the equations in previous sections 3.2 and 3.3 have been removed. The section 3 has been drastically shortened.

P20, L31: CALIOP dust PDR is 30%! CALIOP is measuring at 532 nm, you are measuring at 355nm, and the PDR is then 25%, see the SAMUM and SALTRACE papers of Gross et al. (in Tellus, 2011 and in ACP, 2015). Illingworth is focusing on 355 nm (wavelength of the EarthCARE lidar).
Yes, we have added PDR at 532 nm for the clarity, and add related information:
"(the related PDR at 355 nm is ~25% as proposed in Groß et al., 2015)"
We have also changed the related reference paper.

P21: Do we need Figs. 11 and 12 in the paper?
P22: Fig13? Do we need that?
We have removed these figures and put them in the *Supplement*. We have shortened the discussion on the upper layer (about the mixing dust). The previous sections 4.2.1 and 4.2.2 are now grouped as a new section 4.2.2, we added some discussion on the warehouse fire smoke plum in new section 4.2.1.

The shorter the paper (and compact) the more interesting and attracting.

Analysis of a warehouse fire smoke plume over Paris by N_2-Raman lidar and optical thickness matching algorithm~~Optical thickness matching algorithm applied to the case study of an accidental fire smoke plume over the Paris area with N_2 Raman lidar~~

Xiaoxia Shang[1,*], Patrick Chazette[1], and Julien Totems[1]

[1]Laboratoire des Sciences du Climat et de l'Environnement (LSCE), Institut Pierre Simon Laplace (IPSL), CEA-CNRS-UVSQ, UMR 8212, Gif-sur-Yvette, France
[*]now at: Finnish Meteorological Institute, P.O. Box 1627, 70211, Kuopio, Finland

Correspondence to: Xiaoxia Shang (xiaoxia.shang@fmi.fi)

Abstract. A smoke plume, coming from an accidental fire in a textile warehouse in the north of Paris, covered a significant part of the Paris area on 17 April 2015 and seriously impacted the visibility over the megalopolis. This exceptional event was sampled with an automatic N_2-Raman lidar, which operated 15 km south of Paris. The industrial pollution episode was concomitant with a long-range transport of dust aerosols raised from Sahara, and with the presence of an extended stratus cloud cover. The analysis of the ground-based lidar profiles therefore required the development of an original inversion algorithm, using a top-down aerosol optical thickness matching (TDAM) approach. This study is, to the best of our knowledge, the first lidar measurement of ~~an accidental fire~~ a fresh smoke plume, emitted only a few hours after an accidental warehouse fire. Vertical profiles of the aerosol extinction coefficient, depolarization and lidar ratio are derived to optically characterize the aerosols that form the plume. We found a lidar ratio close to 50 ± 10 sr for this fire smoke aerosol layer. The particle depolarization ratio is low, ~1 ± 0.1%, suggesting the presence of either small particles or spherical ~~particles and therefore highly~~ hydrated aerosols in that layer. A Monte Carlo algorithm was used to assess the uncertainties on the optical parameters, and to evaluate the TDAM algorithm.

Keywords: accidental fire, aerosols, Raman lidar, lidar ratio, depolarization ratio, Raman lidar inversion, TDAM

1 Introduction

Accidental fires cause casualties and significant property damages. In France, one house fire occurs every 2 minutes, adding up to 263 000 domestic fires each year, causing about 100 deaths and 10 000 injuries (http://iaaifrance.fr/). These fires also emit large amounts of gases and aerosols, which are detrimental to human health and degrade visibility. The aerosols have a notable role in cloud formation and in the atmospheric radiative budget (Kanitz et al., 2013). Concerning accidental fires, the meteorological situation has an important role in fire and smoke propagation, especially wind force and direction. In return, fires influence the dynamics and the chemistry of the atmosphere, mainly in the atmospheric boundary layer (ABL) and the

low free troposphere. Modelling tools are needed to predict regional aerosol emissions from large fires and analyse emergency policy options. However, the characterization of fire emissions remains incomplete, mainly due to the difficulty of obtaining young smoke samples. Their unpredictability poses an obvious challenge to perform chemical and meteorological measurements.

Lidar is an efficient technique for the detection of various types of particles along the altitude, such as ash, air pollution, dust, and biomass burning aerosols (Ansmann et al., 2012; Chazette et al., 2007, 2012; Mattis et al., 2010; Müller et al., 2007; Royer et al., 2011; Weitkamp, 2005). Lidar-derived parameters can be effective constraints for chemical-transport models (Binietoglou et al., 2015; Haustein et al., 2009; Wang et al., 2014). Raman lidars, in particular, are becoming well-established tools that are used in the study of numerous areas of importance in the atmospheric sciences (Ansmann et al., 1992; Behrendt et al., 2007; Di Girolamo, 2004; Whiteman, 2003). The use of both Raman- and elastic-backscatter lidar signals allows the independent retrieval of the aerosol extinction and backscatter coefficients (e.g. Ansmann et al., 1992). This technique also enables the retrieval of the extinction-to-backscatter ratio, also called lidar ratio (LR), and the linear particle depolarization ratio (PDR). LR is considered an important criterion to analyse atmospheric aerosols, as it depends on their single scattering albedo and backscatter phase function, and is thus a function of size distribution and chemical composition. PDR provides information on the shape of the scattering particles, allowing the identification of several aerosol types.

Raman lidar data processing remains a complex matter. Three kinds of algorithms are available: 1) single-layer aerosol optical thickness (AOT) constrained Klett inversion, which is a conventional approach based on the Klett algorithm (Klett, 1981), using the N_2-Raman AOT to choose a column-equivalent LR (Ansmann et al., 1990, 1992); 2) standard Raman inversion, based on the numerical derivative of the N_2-Raman channel to retrieve the extinction profile, but introducing noise (Pappalardo et al., 2004; Whiteman, 1999); 3) Raman-constrained regularization, such as the Tikhonov method (Tikhonov and Arsenin, 1978), solving the lidar equation to retrieve simultaneously the aerosol extinction and backscatter coefficient profiles (Royer et al., 2011; Shcherbakov, 2007). As an intermediate, Ansmann (2006) applied a two-layer approach of the Klett method to determine the pair of column lidar ratios for the boundary layer and for the lofted free tropospheric aerosol layer. Yet all these approaches are based on the premise that the elastic channel maximum range can reach an altitude where the backscattered signal is dominated by its molecular contribution (with pure Rayleigh scattering), so as to normalise the signal. We will hereafter call this altitude the Rayleigh zone. One cannot invert the lidar profile if low clouds obstruct the signal or if aerosol layers are present within the hypothetic Rayleigh zone. Moreover, in the presence of a plume from a large fire, it is very common to observe the formation of clouds inside or at the top of the plume, since a fire releases large amounts of water vapour in the atmosphere. The strong AOT of the plume may significantly limit the lidar maximum range, inducing a marked decrease of the signal to noise ratio in the Rayleigh zone. Thus, it may be more interesting to find a reference at a lower altitude to invert the lidar vertical profiles.

On 17 April 2015, we were able to sample ~~an accidental fire~~ a freshly emitted smoke plume from an accidental fire using a N_2-Raman lidar located at Palaiseau (48°42’23"N, 2°13’22"E), ~15 km south of Paris. This fire, of great magnitude, occurred ~5 km north of Paris in a 12000 m^2 textile warehouse located in the commercial area of La Courneuve (48°55'52"N, 2°23'52"E).

The warehouse was totally burned down. To analyse the lidar data recorded during this event, we had to develop a new Raman lidar inversion approach for ground-based measurements, which we call hereafter the top-down aerosol optical thickness matching (TDAM) approach, based on the Klett algorithm. TDAM makes it possible to retrieve the LR profiles with more vertical detail, even when a Rayleigh zone cannot be reached by the lidar.

This paper is organized as follows. In section 2, we introduce the accidental fire event and lidar instrument. In section 3 we recall the theory by presenting the equations and the basic variables associated to N_2-Raman lidar analysis. In the same section, we then present some standard inversions and introduce our new TDAM approach. An uncertainty study is also proposed at the end of that section. The application of TDAM to the warehouse fire smoke plume that passed over the ground-based lidar is discussed in section 4. Section 5 is devoted to the conclusion.

2 Accidental fire and its sampling from ground-based N_2-Raman lidar

2.1 Accidental fire of a warehouse

On 17 April 2015, a violent fire broke out around 2 pm local time (1200 UTC), in a 12 000 m^2 two-storey textile and footwear warehouse in La Courneuve, Seine-Saint-Denis, France (48°55'52"N 2°23'52"E, Figure 1~~Figure 1~~). The plume quickly rose in the lower free troposphere, just above the ABL, by pyro-convection. Black smoke covered the north area of Paris, as shown in Figure 1~~Figure 1~~(b). With a wind speed of ~22 km h^{-1}, the smoke plume rapidly spread from the north-northeast to the south-southwest of Paris. There were no casualties, but property damages were assessed around 40 million Euros. Around 150 firemen and 40 fire trucks participated in the fire fighting. The burning materials were mainly plastic, cloth, wood, paper, etc. (video of the fire at https://www.youtube.com/watch?v=0hC52-pEmu8). The societal impact was also rather important, as the traffic was severely disrupted on numerous highways and railways of the northern Paris area during ~10 hours. A strong smell of smoke and burned plastic spread throughout Paris from that fire and reached the location of the ground-based lidar around 5 pm local time.

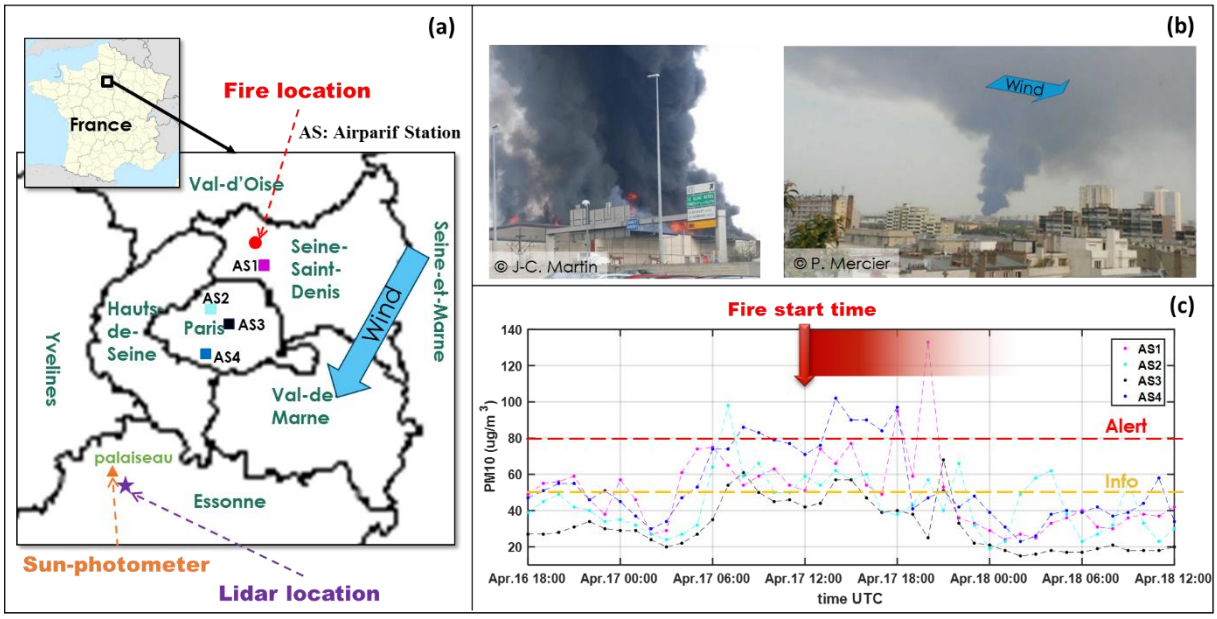

Figure 1. (a): Locations of the textile warehouse on fire (red circle), of lidar instruments (purple pentagram), and of sun-photometer (orange triangle); (b): photo of the smoke plume from near (left) and far (right) distance; (c): in situ measurements of PM_{10} from 4 Airparif stations (locations shown in (a)). The alert / information values are also given in red / yellow dashed line.

2.2 Instrument: N_2-Raman lidar

The N_2-Raman lidar LAASURS (Lidar for Automatic Atmospheric Surveys using Raman Scattering) was put into operation in Palaiseau (48°42'23"N 2°13'22"E, Figure 1~~Figure 1~~a), southwest of Paris, to sample the fire smoke plumes. The direct distance between the locations of the fire and the lidar site is ~28 km.

LAASURS is already well described and validated by Royer et al. (2011) and Chazette et al. (2012). Its characteristics are summarized in Table 1~~Table 1~~; it can be remotely controlled and can work under almost all weather conditions thanks to an air conditioning system and a funnel equipped with air blowers above the optical windows (Figure 2~~Figure 2~~). LAASURS uses an emission wavelength of 355 nm and is designed to fulfil eye-safety conditions at its output. It is composed of two reception channels: one dedicated to the measurement of the co- and cross-polarized signals at ~355 nm and the other to the inelastic nitrogen Raman backscattered signal at ~387 nm. Using a high-speed digitizer card with 200 MHz sampling frequency, ~~It~~ it enables the retrieval of aerosol optical properties and atmospheric structures with an initial/final resolution of 0.75/45 m along the line of sight.

Table 1. Characteristics of LAASURS

Laser type	**Nd:YAG**
	20 Hz
	16 mJ @355 nm

Reception channels	Elastic // (355 nm) Elastic ⊥ (355 nm) N_2-Raman (387 nm)
Reception diameter	15 cm
Field-of-view	~ 2 × 0.67 mrad
Detector	Photomultiplier tubes
Filter bandwidth	0.3 nm
Raw/final vertical resolution	0.75 m / 45 m

Figure 2. The N_2-Raman lidar LAASURS system at the Palaiseau site.

2.3 Raw observations from Lidar

The 10-hour lidar observations of the atmosphere following the fire event are presented in Figure 3~~Figure 3~~, using the temporal evolutions of vertical profiles of both the elastic range-corrected signal (S_{λ_E}) and volume depolarization ratio (VDR). Three main aerosol layers can be easily located in the low troposphere: i) the ABL during the day and the nocturnal layer (NL) during the night, under ~1.2 km amsl (above mean see level), ii) a thin non-depolarizing layer close to 1.2 km amsl with a strong backscatter signal (smoke layer), and iii) a more depolarizing layer between 1.8 and 3 km amsl. The lidar signals are drawn with a time resolution of 1 min, and a vertical resolution of 45 m. During this event, there are a significant amount of profiles

impacted by low clouds, which makes the lidar inversion a challenge. Also, a good vertical resolution of lidar parameters is required to investigate the very thin smoke layer.

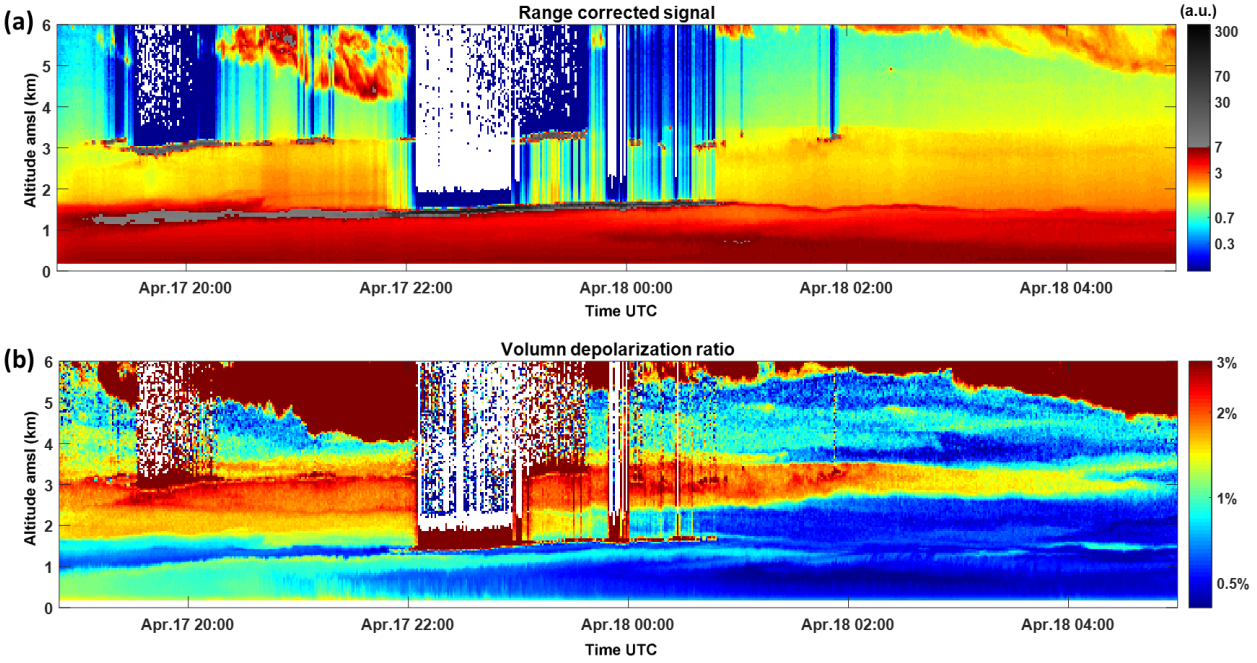

Figure 3. Time series, from 17 April 2015, 1850 UTC to 18 April 2015, 0500 UTC, of the profiles of (a) elastic range-corrected signal (S_{λ_E}), and (b) volume depolarization ratio (VDR~~, bottom panel~~).

3 Algorithms

3.1 ~~Lidar equations~~Basic lidar theory

Starting from the well-known lidar equation (Measures, 1984), the backscattered lidar signal can be corrected for the sky background, the solid angle and the overlap function to obtain the range-corrected lidar signal (RCLS) S_λ. The RCLS of the elastic (E) and the Raman (R) channel are expressed at altitude z as

$$S_{\lambda_E}(z) = K_{\lambda_E} \cdot \left[\beta_{\lambda_E}{}^{mol}(z) + \beta_{\lambda_E}{}^{aer}(z)\right] \cdot \exp\left\{-2\int_0^z \left[\alpha_{\lambda_E}{}^{mol}(z') + \alpha_{\lambda_E}{}^{aer}(z')\right] \cdot dz'\right\} \quad (1)$$

$$S_{\lambda_R}(z) = K_{\lambda_R} \cdot N_{\lambda_R}(z) \cdot \frac{d\sigma_{\lambda_R}(\pi)}{d\Omega} \cdot \exp\left\{-\int_0^z \left[\alpha_{\lambda_E}{}^{mol}(z') + \alpha_{\lambda_E}{}^{aer}(z') + \alpha_{\lambda_R}{}^{mol}(z') + \alpha_{\lambda_R}{}^{aer}(z')\right] \cdot dz'\right\} \quad (2)$$

where λ_E and λ_R designate the emitted wavelength (λ_E = 354.67 nm) and the first Stokes vibrational N_2-Raman wavelength (λ_R = 386.63 nm), respectively. The instrumental constant K_λ contains all altitude-independent system parameters. N_{λ_R} is the nitrogen molecule number density, $d\sigma_{\lambda_R(\pi)}/d\Omega$ is the range-independent differential Raman cross section for the backward direction. α and β are the molecular (*mol*) or aerosol (*aer*) extinction and backscatter coefficients, respectively. The molecular extinction (α^{mol}) and backscatter (β^{mol}) coefficients can be calculated from climatological air mass models or radiosonde

measurements. They are determined in this study with a polynomial approximation as in Nicolet (1984) using a reference atmospheric density calculated from ancillary measurements (Chazette et al., 2010); $\beta_{\lambda_E}{}^{mol}$ is expressed as $3k_f\alpha_{\lambda_E}{}^{mol}/8\pi$, with the King factor of air k_f (King, 1923). The aerosol extinction (α^{aer}) is assumed to be proportional to $\lambda^{-Å}$,

$$\frac{\alpha_{\lambda_R}{}^{aer}}{\alpha_{\lambda_E}{}^{aer}} = \left(\frac{\lambda_R}{\lambda_E}\right)^{-Å} \quad (3)$$

where the Ångström exponent *Å* (Ångström, 1964) is considered to be a constant depending on the aerosol nature. This value can be obtained from external data such as a sun-photometer (Dubovik et al., 2002). Note that *Å*~0 corresponds to large dust or cirrus particles, *Å*~1.5 corresponds to small smoke particles, and sulfate aerosols are associated with the higher value *Å*~2. Thus, in the absence of external data, an average value of 1 can be used.

3.2 Retrieved aerosol optical parameters

The aerosol optical thickness (AOT, AOT_λ) between two altitudes z_i and z_j at the wavelength λ is defined as the integration of the aerosol extinction coefficient (AEC, $\alpha_\lambda{}^{aer}$) on the altitude range $[z_i, z_j]$ ($\int_{z_i}^{z_j}\alpha_{\lambda_E}{}^{aer}(z')\cdot dz'$) and can be derived directly using the Raman channel signal from Eq.2 (Royer et al., 2011).

$$AOT_{\lambda_E}(z_i,z_j) = \frac{\ln\frac{S_{\lambda_R}(z_j)N_{\lambda_R}(z_i)}{S_{\lambda_R}(z_i)N_{\lambda_R}(z_j)} + \int_{z_i}^{z_j}\left[\alpha_{\lambda_E}{}^{mol}(z\prime)+\alpha_{\lambda_R}{}^{mol}(z\prime)\right]\cdot dz\prime}{-\left[1+\left(\frac{\lambda_N}{\lambda_E}\right)^{-Å}\right]} \quad (4)$$

For a chosen reference altitude (z_0), the aerosol backscatter coefficient (ABC, $\beta_\lambda{}^{aer}$) at altitude z can be derived using either the ratio of the elastic signals which is corrected from the molecular extinction contribution (Royer et al., 2011), or the ratio of the elastic and the Raman backscattered signals (Ansmann et al., 1992; Whiteman et al., 1992):

$$\beta_{\lambda_E}{}^{aer}(z) = \left[\beta_{\lambda_E}{}^{mol}(z_{ref}) + \beta_{\lambda_E}{}^{aer}(z_{ref})\right]\cdot\frac{S_{\lambda_E}(z)}{S_{\lambda_E}(z_{ref})}\cdot\exp\left\{-2\int_{z}^{z_{ref}}\alpha_{\lambda_E}{}^{mol}(z')\cdot dz'\right\}\cdot\exp\left\{-2\cdot AOT_{\lambda_E}(z,z_{ref})\right\} - \beta_{\lambda_E}{}^{mol}(z) \quad (5)$$

An assumption about the reference value $\beta_{\lambda_E}{}^{aer}(z_{ref})$ is needed. Usually, the reference altitude z_{ref} is chosen in a Rayleigh zone where the aerosol load is negligible, i.e. $\beta_{\lambda_E}{}^{mol}(z_{ref}) \gg \beta_{\lambda_E}{}^{aer}(z_{ref})$.

For lidar systems with co- and cross- polarized channels, the volumetric depolarization ratio (VDR) and linear particle depolarization ratio (PDR) can be derived following the procedure described in Chazette et al. (2012). The RCLS for co-polarization ($S_\parallel$) and cross-polarization ($S_\perp$) can be expressed by Eq.1, with the instrumental constant $K_\parallel$ and $K_\perp$, respectively. The subscript λ_E is omitted here. The cross-calibration coefficient $K_\parallel/K_\perp$ can be accessed by a normalization of the lidar signals within a Rayleigh zone. During our experiment, VDR and PDR are determined following the procedure described in Chazette et al. (2012).

$$VDR(z) = \frac{K_\parallel}{K_\perp}\cdot\frac{S_\perp(z)}{S_\parallel(z)} \quad (6)$$

$$PDR(z) = \frac{\beta^{mol}(z)\cdot\left(VDR^{mol} - VDR(z)\right) - \beta^{aer}(z)\cdot VDR(z)\cdot(1+VDR^{mol})}{\beta^{mol}(z)\cdot(VDR(z) - VDR^{mol}) - \beta^{aer}(z)\cdot(1+VDR^{mol})} \quad (7)$$

As the PDR is a physical parameter retrieved with a high uncertainty when there are few aerosol particles, its calculation in this study is performed only for layers where the AEC is at least 0.01 km^{-1}.

3.3 Overview of some existing algorithms to retrieve the lidar ratio

The lidar ratio (LR, also called particle extinction-to-backscatter ratio) is determined by the ratio of two unknowns, α^{aer} and β^{aer}, of the lidar equation. ÷

$$LR(z) = \frac{\alpha^{aer}(z)}{\beta^{aer}(z)} \quad (8)$$

The LR depends on the complex refractive index, size, shape and orientation of aerosols (Sasano et al., 1985). The column-equivalent lidar ratio (CLR) between two altitudes z_i and z_j ($z_j > z_i$) is also widely used. As an AEC weighted average of LR along the altitude, it is defined as:

$$CLR(z_i, z_j) = \frac{\int_{z_i}^{z_j} \alpha^{aer}(z')\cdot dz'}{\int_{z_i}^{z_j} \frac{\alpha^{aer}(z')}{LR(z')}\cdot dz'} \quad (9)$$

The Klett algorithm (Klett, 1981, 1985) is widely used for the inversion of the elastic lidar signal. Formulating Eq.1 as a Bernoulli equation, its solution can be written as:

$$\frac{\alpha_{\lambda_E}^{aer}(z)}{LR(z)} + \beta_{\lambda_E}^{mol}(z) = \frac{S_{\lambda_E}(z)\cdot Q(z)}{\frac{S_{\lambda_E}(z_{ref})}{\beta_{\lambda_E}^{aer}(z_{ref}) + \beta_{\lambda_E}^{mol}(z_{ref})} + 2\int_z^{z_{ref}} S_{\lambda_E}(z')\cdot Q(z')\cdot LR(z')\cdot dz'} \quad (10)$$

with $Q(z)$ a correction function due to the differential molecular optical thickness calculated from the vertical profile of the molecular extinction coefficient:

$$Q(z) = exp\left(2\cdot\int_z^{z_{ref}}\left[\beta_{\lambda_E}^{mol}(z')\cdot LR(z') - \alpha_{\lambda_E}^{mol}(z')\right]\cdot dz'\right) \quad (11)$$

There are three unknowns in this solution to the lidar equation (Eq.10): $\alpha_{\lambda_E}^{aer}(z)$, $LR(z)$ and $\beta_{\lambda_E}^{aer}(z_{ref})$.

The main Raman inversion methods, yielding retrievals of LR, can be classified as 3 types of algorithms :discussed in the following.

(1)

3.3.1 Single-layer AOT constrained Klett algorithm

One option to go further is to assume that LR is constant against altitude. Another constraint is necessary to solve Eq.10, which is often chosen as the AOT of the entire aerosol vertical column (noted as AOT_0). The N_2 Raman channel can provide AOT_{ref} when its maximum range reaches the chosen reference altitude z_0. Otherwise, an external constraint should be considered. It can be the AOT derived from a sun photometer (e.g. Chazette et al., 2016) or spaceborne radiometer (Ansmann et al., 1990; Chazette et al., 2010; Dieudonné et al., 2015). A bisection method is then used to retrieve an altitude independent LR, as proposed in Raut and Chazette (2007). An initial value LR (e.g. 50 sr) and a step for each iteration (e.g. 3 sr) are chosen. This

~~*LR* should be increased (decreased) if the retrieved AOT is smaller (larger) than the targeted AOT_0. It can also be a window algorithm as proposed in Dieudonné et al. (2015): the extinction profile is inverted using several *LR* values (e.g. 13 values of *LR* distributed from 10 to 130 sr). Then, the interval is narrowed between the two *LR* values that produce the best AOT and the process is repeated. Both procedures can be considered convergent when the agreement between the retrieved AOT and AOT_0 is better than 10^{-4}.~~ The main error sources are well known and are mainly due to the vertical heterogeneity of the aerosol layers. The altitude-independent LR can be poorly representative of the actual LR profile, especially in presence of multiple scattering layers composed of different types of aerosol (e.g. dust, pollution and sea-salt aerosols, ~~(~~Chazette et al., 2016~~)~~).

According to the sensitivity study carried out by Royer et al. (2011), for the same N_2-Raman lidar presented in section 2.2, the relative error on the altitude-independent LR ranging between 4 and 18% (16 to 100 %) during night-time (day-time) for AOT values ranging from 0.1 to 0.5. Note that Ansmann (2006) found a difference in the altitude-independent LR of up to 20% between the single-layer Klett solutions from spaceborne and ground-based lidar.

~~3.3.2~~ (2) Standard Raman inversion.

Mathematically, the AEC ~~(α^{aer})~~ can be retrieved directly by differentiating the Raman-derived AOT profile ~~from Eq.4~~. ~~However, the noise on the Raman lidar signal can produce sizeable errors when performing this derivation. Therefore, smoothing techniques are necessary, such as low-pass derivative filters (Dieudonné et al., 2015), Kaiser filters (Kaiser and Reed, 1977), or Savitzky–Golay filters (Press et al., 1992). If one can calculate the ABC (β^{aer}, Eq.5) using the method described in section 3.2, the LR profile can then be retrieved (Eq.8).~~

The distinction between algorithms of standard Raman inversion mainly concerns data-smoothing techniques and the evaluation of a numerical derivative (Pappalardo et al., 2004; Whiteman, 1999). Pappalardo et al. (2004) reported on the inter-comparison of several standard Raman inversions in the EARLINET network, which shows a mean deviation of LR within 20% in the ABL, and within 15% for a lofted aerosol layer.

~~3.3.3~~ (3) Raman-constrained regularization.

~~The numerical differentiation is known to be difficult. Small perturbations in the AOT profile to be differentiated may lead to considerable errors in the computed derivative. A regularization theory was developed to derive an efficient and numerically stable estimator of the actual solution (Tikhonov and Arsenin, 1978).~~

~~The core principle is to solve the system of Eqs. 1 and 2 in which the AOT has been replaced by the product of the ABC and the LR (Eqs. 4 and 8):~~

$$AOT_{\lambda_E}(z_i, z_j) = \int_{z_i}^{z_j} LR(z') \cdot \beta_{\lambda_E}^{aer}(z') \cdot dz' \quad (12)$$

~~Several regularization methods are available, such as the Tikhonov regularization (Tikhonov and Arsenin, 1978), the Maximum entropy regularization (Mohammad-Djafari et al., 2002), the Truncated singular value decomposition method (Hansen and Christian, 1990), the Total variation regularization (Boyd and Vandenberghe, 2004), etc.~~ The regularization method most commonly used for Raman lidar processing is the Tikhonov regularization method (Royer et al., 2011;

Shcherbakov, 2007). Shcherbakov (2007) reports a regularized algorithm (based on theory in Tikhonov and Arsenin, 1978~~Tikhonov's~~), which improved the quality of the Raman lidar data processing compared to the standard Raman inversion. The retrieved LR profile has reduced root-mean-square errors but does not follow strong variations of the actual LR, especially at the boundaries between layers, and its smoothness gives a false impression of precision in zones with low signal to noise ratio (SNR). The Tikhonov approach is inherently an optimal estimator for the ABC, and not for the LR.

~~3.4~~3.2 The top-down aerosol optical thickness matching (TDAM) algorithm

All the above approaches are based on the assumption that the aerosol load in the reference zone is negligible. However, because of clouds or thick aerosol loads or strong daylight background limiting the maximum usable range of the backscatter signals, or the presence of aerosols high in the free troposphere, there are cases in which a pure Rayleigh reference zone cannot be reached or does not exist (e.g. profiles with clouds or dust plumes above the ABL in this study). Moreover, we have discussed the limitations of regularized approaches that we cannot retrieve detailed information due to a vertical resolution unsuitable for a thin aerosol layer (e.g. the warehouse ~~accidental~~ fire smoke aerosol layer in this study). For ground-based N_2-Raman lidar, a new algorithm has been developed to solve these problems and will be described in this section. In the following, the parameters without subscripts relate to the emitted wavelength (λ_E).

~~3.4.1~~3.2.1 Reference zone and related optical parameters

The lidar profile is shared in several atmospheric layers indexed from $i = 1$ to n, with the lowest index ($i = 1$) corresponding to the maximum usable range of the signal, and i increasing downwards to the ground level. Note that the layers are not necessarily equidistant. Whether the Raman channel reaches a pure Rayleigh zone or not, we choose the reference zone in the altitude range of $[z_1, z_0]$, named as the 1st altitude interval, in which the AEC is considered as constant against the altitude (Figure 4~~Figure 4~~). Figure 5~~Figure 5~~ gives an illustration of the method, using an actual lidar profile acquired during the fire smoke event (at 2120 UTC). To estimate the AEC in the reference zone, due to a weak SNR, a least mean square approach is applied on the normalised N_2-Raman lidar signal, after correction of the molecular contributions:

$$R_{\lambda_R}(z) = \frac{S_{\lambda_R}(z)\cdot N_{\lambda_R}(z_0)\cdot\exp\left\{\int_0^z\left[{\alpha_{\lambda_E}}^{mol}(z\prime)+{\alpha_{\lambda_R}}^{mol}(z\prime)\right]\cdot dz\prime\right\}}{S_{\lambda_R}(z_0)\cdot N_{\lambda_R}(z)\cdot\exp\left\{\int_0^{z_0}\left[{\alpha_{\lambda_E}}^{mol}(z\prime)+{\alpha_{\lambda_R}}^{mol}(z\prime)\right]\cdot dz\prime\right\}}, \quad (3)$$

as proposed by Chazette et al. (2016). This ratio is proportional to the aerosol transmission in the 1st altitude interval, where the AEC is considered as constant, so that

$$R^E_{\lambda_R}(z) = \exp\left\{-\left[1+\left(\frac{\lambda_N}{\lambda_E}\right)^{-\text{Å}}\right]\cdot {\alpha_{ref}}^{aer}\cdot(z-z_0)\right\}, z\in[z_1,z_0], \quad (4)$$

Hence, the estimator $\widehat{{\alpha_{ref}}^{aer}}$ of the AEC at the reference altitude is derived from

$$\widehat{{\alpha_{ref}}^{aer}} = \underset{{\alpha_{ref}}^{aer}}{\operatorname{argmin}}\left\|R_{\lambda_R}(z)-R^E_{\lambda_R}(z)\right\|^2, z\in[z_1,z_0], \quad (5)$$

The computation of the LR in the 1st altitude interval (LR_1) needs a 2nd altitude interval [z_2, z_1], with $z_2 < z_1$. The altitude z_2 is chosen to verify the following constraint on the partial AOT (PAOT) between z_2 and z_0:

$$AOT(z_2, z_0) \geq 0.05. \quad (6)$$

The PAOT is derived from the Raman channel profile ~~(Eq.4)~~. The ABC at the reference altitude is given by

$$\beta_{\lambda_E}{}^{aer}(z_{ref}) = \frac{1}{LR_1}\frac{AOT(z_1,z_0)}{z_0-z_1}, \text{ with } z_{ref} = \frac{z_0+z_1}{2}. \quad (7)$$

It is used as an initial value to constrain ~~Eq.10~~the Klett inversion (e.g. Eq.12 in Royer et al., 2011). We assume that $LR_2 = LR_1$, between z_2 and z_0. Hence, an analytical solution exists and is given by

$$\widehat{LR_1} = \widehat{LR_2} = \frac{R_{\lambda_E}(z_2)\cdot\frac{AOT(z_1,z_0)}{(z_0-z_1)}\cdot\exp[-2\cdot AOT(z_2,z_0)] - \frac{AOT(z_2,z_0)}{(z_0-z_2)}}{\beta_{\lambda_E}{}^{mol}(z_2) - R_{\lambda_E}(z_2)\cdot\beta_{\lambda_E}{}^{mol}(z_{ref})\cdot\exp[-2\cdot AOT(z_2,z_0)]} \quad (8)$$

where R_{λ_E} is the ratio of elastic lidar signal after correction of the molecular transmission:

$$R_{\lambda_E}(z) = \frac{S_{\lambda_E}(z)\cdot\exp\left\{2\int_0^z\left[\alpha_{\lambda_E}{}^{mol}(z')\right]\cdot dz'\right\}}{S_{\lambda_E}(z_0)\cdot\exp\left\{2\int_0^{z_0}\left[\alpha_{\lambda_E}{}^{mol}(z')\right]\cdot dz'\right\}} \quad (9)$$

If the solution does not converge to plausible LR values (between 20 and 120 sr), the 2nd altitude interval is enlarged by one resolution step of the lidar profiles, and so on.

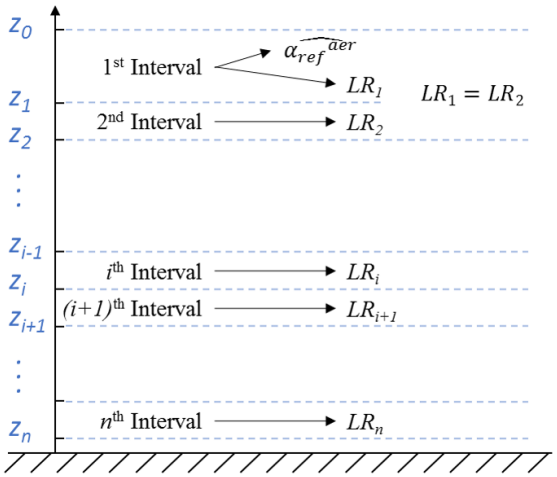

Figure 4. Diagram of i^{th} (i = 1, 2, … , n) altitude interval for the altitude range [z_i , z_{i-1}], using in TDAM (top-down aerosol optical thickness matching) algorithm.

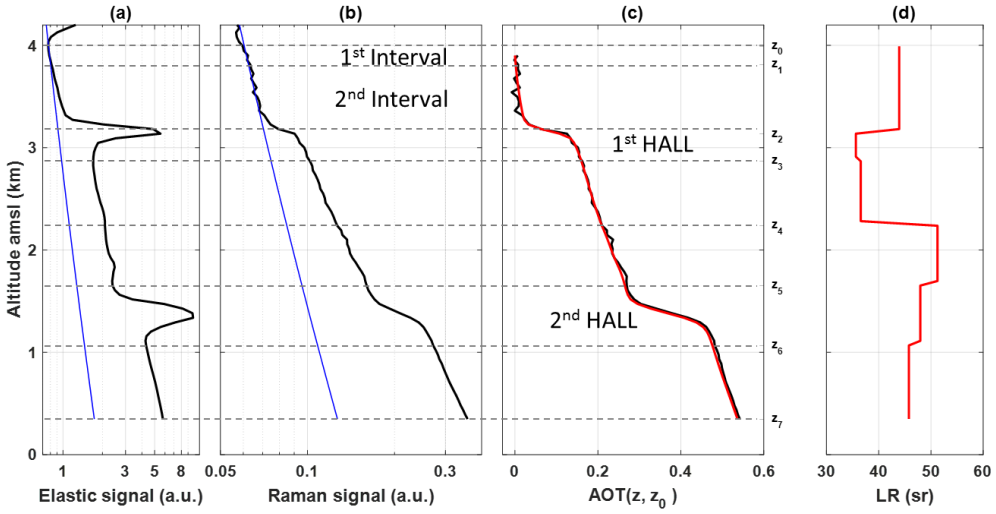

Figure 5. Example for the demonstration of the TDAM (top-down aerosol optical thickness matching) algorithm, which is an actual lidar measurement at ~17 April 2120 UTC (c.f. Figure 3~~Figure 3~~). (a) Range-corrected Elastic signal (black) with fitted molecular elastic signal (blue). (b) Range-corrected Raman signal (black) with fitted molecular Raman signal (blue). (c) Raman-derived AOT profile (black) with retrieved AOT profile using TDAM (red). Altitudes determining layers are shown by dotted lines, from which we can find the 1st altitude interval [z_1, z_0], the 2nd altitude interval [z_2, z_1], and the i^{th} altitude interval [z_{i+1}, z_i]. The 2 heavy aerosol load layer (HALL) are also shown. (d) Retrieved LR profile using TDAM algorithm**.**

~~3.4.2~~3.2.2 Profiles of the aerosol optical parameter derived from the N_2-Raman lidar

At this stage, the goal is to estimate profiles of ${\alpha_{\lambda_E}}^{aer}(z)$ and $LR(z)$ ~~(see Eq.10)~~, using the LR and AEC previously retrieved at the reference altitude. Below the 1st and 2nd altitude intervals, we identify *n-2* successive homogeneous layers (see Figure 4~~Figure 4~~), and the LR inside each layer is assumed to be altitude-independent. Different methods can be used for this step. The easiest way is using a constant altitude interval (e.g. one LR value per 1 km). The altitude interval can also be defined considering a minimal value of PAOT (e.g. 0.1) to be reached in each interval. Indeed, the LR is meaningless for layers where the aerosol load is too small, this argues for sufficiently high PAOTs in each altitude range. Note that a thin layer *i* of strong PAOT can also significantly bias the retrieval of the LR value for the remaining *n-i* layers.

In this study, a more evolved method is used to define layers. Firstly, the existence of a "heavy aerosol load layer" (HALL) is checked using the slope of the range-corrected elastic signal, which has a better SNR than the Raman signal. In our example in Figure 5~~Figure 5~~, we find two homogeneous aerosol layers, the first one between z_3 and z_2 and the second one between z_5 and z_6, as HALLs. Furthermore, we considered the ABL as one homogeneous layer. Secondly, we choose a constant AOT increment to determine the other homogeneous layers (Figure 5~~Figure 5~~(c)). In this study we select a value of 0.05 as a compromise between the final vertical sampling of LR and the computation time. Once the different layers, $i = 3,...,n$, are defined, the inversion procedure starts.

The LR in the i^{th} altitude interval, $LR_i = LR(z_i, z_{i-1})$, can be derived following a procedure similar to the one presented in the previous section (Eq.8~~18~~), using the layer PAOT, $AOT(z_i, z_{i-1})$. A LR profile, keeping the estimated values $LR_1,\ldots,LR_{i-1}$ for

the previous layers and testing for LR_i in the new layer m values centred around LR_{i-1}, is used for Klett inversion at this step. The LR_i value best matching the Klett-derived PAOT to the measured value is chosen. We find that iterating (up to 3 times) with m = 7 values and finer increments until the PAOT is found within 10^{-4} yields the best results in terms of precision and computation time.

This procedure is repeated for all the altitude intervals until the ground level is reached. The final estimate of the LR profile of the example considered in Figure 5~~Figure 5~~ is shown in Figure 5~~Figure 5~~d. Using the backward Klett method, we use this LR profile and the range-corrected elastic signal to compute the AOT profile (superimposed in red in Figure 5~~Figure 5~~c), which matches well the AOT retrieved from the N_2-Raman channel.

The TDAM method may be of advantage if the retrieved backscatter coefficient profile indicates pronounced heterogeneities against altitude. It can be used extensively, even for daytime inversions, if the Raman maximum range is sufficient. However, this algorithm cannot be used to generate real-time quick look plots, because it is relatively time consuming (~45 s computation time per profile).

~~3.5~~3.3 Uncertainty sources

The uncertainties on aerosol optical properties retrieved from N_2-Raman lidar measurements are mainly i) bias linked to the effective vertical resolution, ii) bias due to an inaccurate AEC in the reference zone, iii) bias due the assumed model of the molecular contribution, iv) bias due to the assumed Ångström exponent and v) random error associated with the signal noise characterized by the SNR. The main uncertainties of the TDAM method will be discussed in the following. Uncertainty sources are assumed to be independent. Note that an error can be also introduced by temporal averaging during varying atmospheric extinction and scattering conditions, which will be also discussed in the next section for the warehouse fire smoke case study.

An end-to-end simulator was developed for the error study of TDAM method, with the block diagram shown in Figure 6~~Figure 6~~. We developed a similar algorithm when studying the uncertainty sources for a spaceborne lidar dedicated to forest studies (Shang and Chazette, 2015). The input profiles of AEC and LR (AEC_0 and LR_0) can either be the ones retrieved from actual measurements or simulated profiles. They are used to simulate the backscattered lidar signals of both elastic ($\widetilde{S_{\lambda_E}}$) and Raman ($\widetilde{S_{\lambda_N}}$) channels through the "direct model". The instrument parameters are adjusted using actual lidar signals. An atmospheric molecular model is used to provide the molecular contributions. The statistical error study is performed using a Monte Carlo approach as described in Chazette et al. (2001). The main sources of noise were taken into account considering normal statistical distributions, which are introduced by a normal random generator. For each statistical simulation, we used 100 draws, ensuring a normal distribution up to one standard deviation away from the mean value of the parameters. Each statistical realization of the lidar signals was then inverted by the "inverse model" to estimate the aerosol optical parameters. The comparison between these estimators and the initial values was then performed in the "comparison module" to retrieve the bias and standard deviations on the AEC, AOT and LR.

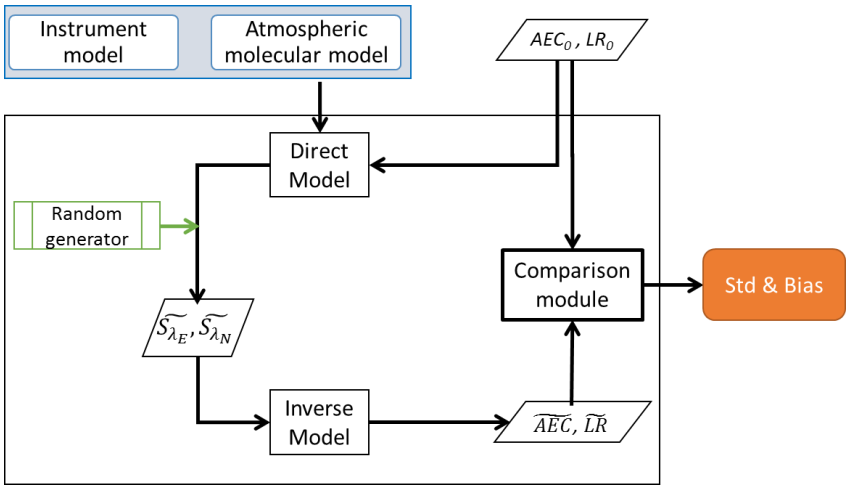

Figure 6. Block diagram of the end-to-end simulator. See text in section 3.3~~3.5~~.

~~3.5.1~~3.3.1 Systematic errors

Systematic errors are mainly associated with the estimated input parameters. The uncertainty on the a priori knowledge of the vertical profile of the molecular contribution, as determined from ancillary data, has been assessed to be lower than 2% as in Chazette et al. (2010) using a comparison between several radiosoundings. The Ångström exponent ($\AA$) used in this study is 1.1. The Aerosol Robotic Network (AERONET) Level 2.0 product from the Palaiseau station near the lidar station (http://aeronet.gsfc.nasa.gov/, Figure 1~~Figure 1~~) is considered, from which the visible (440-675 nm) mean $\AA$ on 17 April is found to be ~1.14 ±0.05, representative of carbonaceous particles. Note that the Ångström exponent for Paris background aerosols is ~1.5 (Chazette and Royer, 2017). Chazette et al. (2014) report that the residual relative uncertainty on LR due to $\AA$ ±0.05 was calculated to be less than 3%. The use of King factor k_f = 1 causes an overestimation of the molecular volume backscatter coefficient of 1.5% at 355 nm (Collis and Russel, 1976). The error due to temporal averaging is not discussed here as it depends substantially on the atmospheric situation and should be studied separately for each study period.

~~3.5.2~~3.3.2 Bias linked to the effective vertical resolution and AEC at the reference altitude

In this section, only simulated mean lidar signals are considered for the assessment of the biases linked to the effective vertical resolution and to the AEC at the reference altitude.

Firstly, we check the ability of the TDAM method to resolve two narrow and well-separated structures in the aerosol extinction profile. A step function proposed by Pappalardo et al. (2004) is here used to evaluate the effective vertical resolution. We took into account 7 pairs of AEC profiles with Dirac peaks (the value is equal to zero everywhere except at the height of peaks), which are separated by 4, 6, 8, 12, 18, 22, 26, and 30 points between 2 peaks, respectively. In each case, the LR is set to be 40 for the top peak and 80 for the bottom peak. Using the TDAM method, we retrieved the $\widetilde{AEC}$ and $\widetilde{LR}$, which are then compared with the initial values (AEC_0 and LR_0). We find that TDAM resolves the two peaks of AEC separated by 6 points, which is

related to an effective vertical resolution of 270 m in this study. The relative uncertainty on LR retrieval is ~30% for the pairs with 4 points distance; whereas other relative errors on LR are reasonable (<10%) for pairs with distance bigger than the effective vertical resolution.

Secondly, bias linked to the AEC at the reference altitude is evaluated. A heterogeneous atmosphere is considered here, with 2 superimposed layers with different aerosol loads and types (a Gaussian profile is chosen for each layer): i) a smoke layer (LR_0 = 50 sr) centred at 2 km amsl, with an AOT of 0.3 and a thickness of ~500 m; ii) a polluted boundary layer (LR_0 = 80 sr) with an AOT of 0.2 from ground to 1.7 km amsl. A background aerosol condition is also added, with a constant AEC of 0.05 km^{-1} from 0 to 6 km (LR_0 = 80 sr).

We set the reference zone at 4-5 km, where the correct AEC (${\alpha_{ref}}^{aer}$) should be 0.05 km^{-1}. Several artificial $\widehat{{\alpha_{ref}}^{aer}}$ values from 0 to 0.2 km^{-1} were used for the inversion to assess the relative bias. We found that using 0 instead of 0.05 km^{-1} as the $\widehat{{\alpha_{ref}}^{aer}}$, the LR of the smoke aerosol layer (SAL) will be over-estimated, with a relative bias of +40% in this simulated case. When the $\widehat{{\alpha_{ref}}^{aer}}$ is over-estimated as 0.1 km^{-1} (0.14 km^{-1}), the bias on the LR retrieval is ~-12% (-23%). Note that if one uses the other 3 methods mentioned in section 3.1~~3.3~~ without a correct estimation of $\widehat{{\alpha_{ref}}^{aer}}$ (i.e. 0 instead of the actual ${\alpha_{ref}}^{aer}$), the LR retrieval will probably be overestimated.

~~3.5.3~~3.3.3 Random error due to noise

In this section, we investigate the random error due to the noise on acquired signals, using the end-to-end simulator (Figure 6~~Figure 6~~) based on a Monte Carlo approach. The input profiles of AEC and LR (AEC_0 and LR_0 in Figure 7~~Figure 7~~a,b) are produced by smoothing actual measurements (17 April ~2020 UTC). The reference altitude was selected to be ~4 km amsl, where the ${\alpha_{ref}}^{aer}$ was 0.032 km^{-1} with a LR at the reference altitude (LR_{ref}) of 42 sr. One hundred draws were performed, with the noise level determined from the SNR of the actual lidar signals; the SNR at the reference altitude on Raman channel signal is found to be ~184. One draw of simulated range-corrected elastic and Raman signal are shown in Figure 7~~Figure 7~~c, d. The aerosol layer at ~1.5 km is related to our observed SAL, with an initial column-equivalent lidar ratio (CLR) value of 44 sr.

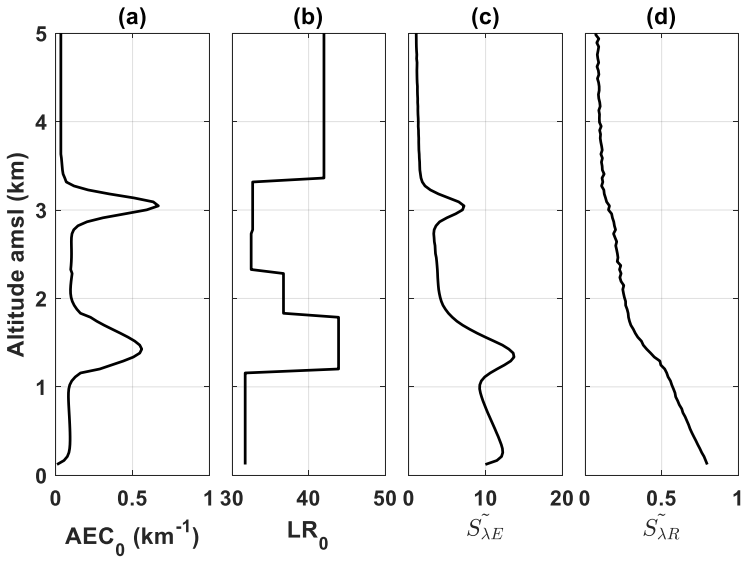

Figure 7. Input profiles of (a) Aerosol extinction coefficient (AEC_0) and (b) lidar ratio (LR_0) for statistical error study. One draw of the 100 simulated profiles of range-corrected (c) elastic signal and (d) Raman signal are shown.

Through the Monte Carlo simulation, we found that for this case, when ${\alpha_{ref}}^{aer}$ and LR_{ref} are assumed to be well known (i.e. fixed as the input values), the total errors (including bias and standard deviation) on the CLR of the SAL (at ~1.5 km amsl) and the ABL (below 1 km amsl) are 1.9 and 2.2 sr, respectively. The errors on the estimation of the ${\alpha_{ref}}^{aer}$ and LR_{ref} are found to be ~0.01 km^{-1} and ~13 sr, which results in more important errors on CLR: 3.4 sr for the SAL and 4.2 sr for the ABL.

To assess the uncertainty on CLR due to random detection processes for lidar signal of different SNR, different levels of noise have been added to the lidar profiles using the normal Random generator. 22 SNR levels were considered in this study, with SNR values at the reference altitude on the N_2-Raman channel signal ranging from 9 to 1840. For each SNR level, 100 statistical draws were simulated and inverted using the end-to-end simulator. Figure 8~~Figure 8~~ show the errors on retrieved parameters due to random detection processes against the SNR at the reference altitude (z_{ref}) on the N_2-Raman channel using TDAM approach. The top panel shows the percentage of inversible profile numbers. We defined "inversible profile" as the one which can be inversed and gives us reasonable optical values (e.g. LR). When the SNR is smaller than 10, we are not able to inverse this lidar profile using the TDAM approach. The middle and bottom panels show the errors on ${\alpha_{ref}}^{aer}$ and CLR of the SAL and ABL due to random detection processes. For SNR under 95, the relative errors on ${\alpha_{ref}}^{aer}$ are higher than ~~100~~40%; whereas the errors on CLR are ~4 or ~8 sr for the SAL and ABL. The error on CLR of SAL is lower than the one of ABL, simply because of larger aerosol load (i.e. larger AEC).

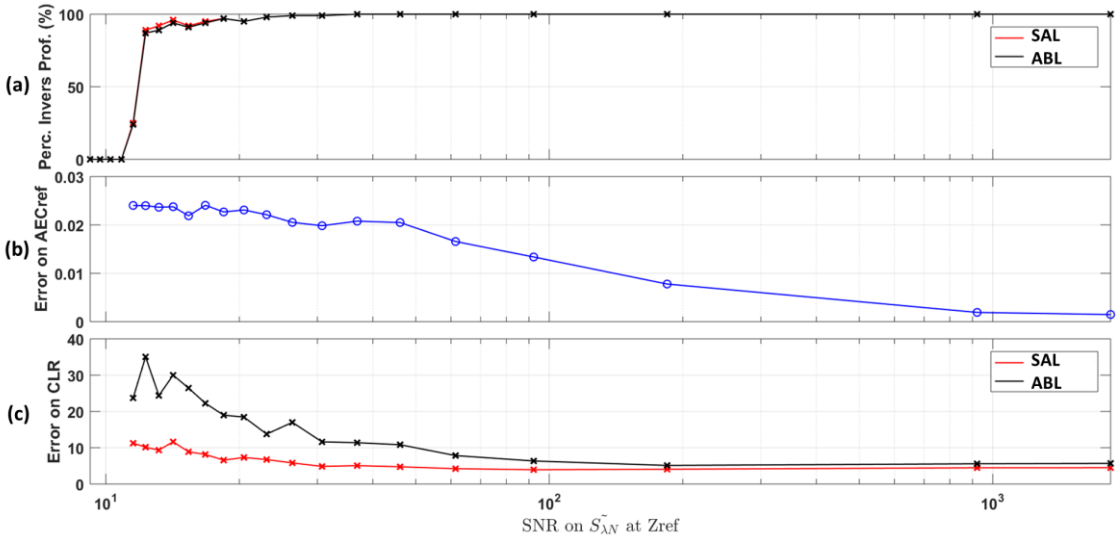

Figure 8. (a) Percentage of inversible profiles, (b) errors on AECref (AEC at the reference altitude, $\alpha_{ref}{}^{aer}$, in km^{-1}) and (c) errors on CLR (column-equivalent lidar ratio, in sr) due to random detection processes against the SNR at the reference altitude (z_{ref}) on the Raman channel ($\widetilde{S_{\lambda N}}$) using TDAM approach. Red and black lines show values for the SAL (smoke aerosol layer, between 1.1-1.8 km amsl) and for the ABL (atmospheric boundary layer, below 1 km amsl), respectively.

4 Aerosol optical properties of ~~Results: application to~~ the warehouse fire smoke plume

4.1 Lidar-derived aerosol optical properties in the low-middle troposphere ~~Lidar-derived aerosol optical properties~~

The lidar observations of the low troposphere following the accidental fire event are analysed using the TDAM approach. Lidar data is time averaged over 60 min to increase the SNR, especially for the N_2-Raman channel. The reference zone of each profile is chosen below the thick stratus cloud. The TDAM algorithm is applied to the average profiles for the whole observation period to retrieve the aerosol optical parameters and mainly the vertical profile of the LR. The LR profiles are then used to invert the 1-min resolution elastic signal to assess the vertical profile of the AEC. As previously explained, the PDR is calculated only for AEC greater than 0.01 km^{-1}, as it is undefined and noisy for lower values. The temporal evolutions of retrieved vertical profiles of both AEC and PDR are shown in Figure 9~~Figure 9~~. Two examples of retrieved vertical profiles are also given in Figure 10~~Figure 10~~, each one is related to 60 profiles of ~1h acquisition time centred on 17 April 2049 UTC or 18 April 0152 UTC. The standard deviations around the mean values are represented by grey areas, showing the uncertainty due to the signal averaging during varying atmospheric extinction and scattering conditions. Two other time periods are selected, when there are no cloud in the considered layers, during which the average optical properties of 3 layers are summarized in Table 2.

We can easily figure out that the ABL or NL are well decoupled from the free troposphere through the intensity of backscattered signal (Figure 3~~Figure 3~~a). Before and after 17 April 2200 UTC, aerosol typing in the first kilometre of atmosphere appears

different with a significant decrease in the PDR from ~3% to ~0.5%. In both cases, the aerosols are likely spherical, as they are associated with a small depolarization ratio. This temporal evolution may be due to aerosols of different origins being advected over time. The LR in the ABL/NL is found to be between 40-70 sr, as usually observed in the Paris area (e.g. Royer et al., 2011).

One thin layer is located just at the top of the ABL/NL, close to 1.2 km amsl. This aerosol layer is associated with a strong AEC (~0.8 ± 0.1 km^{-1}) and a small PDR (~1 ± 0.1%). It is related to the fresh smoke plume coming from the accidental fire. These aerosols are non-depolarizing and therefore very likely to be spherical and composed of water-soluble compounds trapped inside their shell. The LR of the smoke plume is ~50 ± 10 sr. The partial AOT of this layer ranges from 0.1 to 0.3, and dominates the AOT of the full atmospheric column.

The upper, more depolarizing aerosol layer, located between 1.8 and 3 km amsl, presents a PDR of ~8 ± 3%, and a LR ~40 ± 10 sr, which is characteristic of a mix of pollution and dust aerosols. This layer fades in the morning of 18 April. Within this layer, as within the smoke plume, aerosols seem to favour the formation of clouds, which results in an intense backscattered signal (the gray area seen in Figure 3~~Figure 3~~), and pleads for the presence of hydrophilic particles.

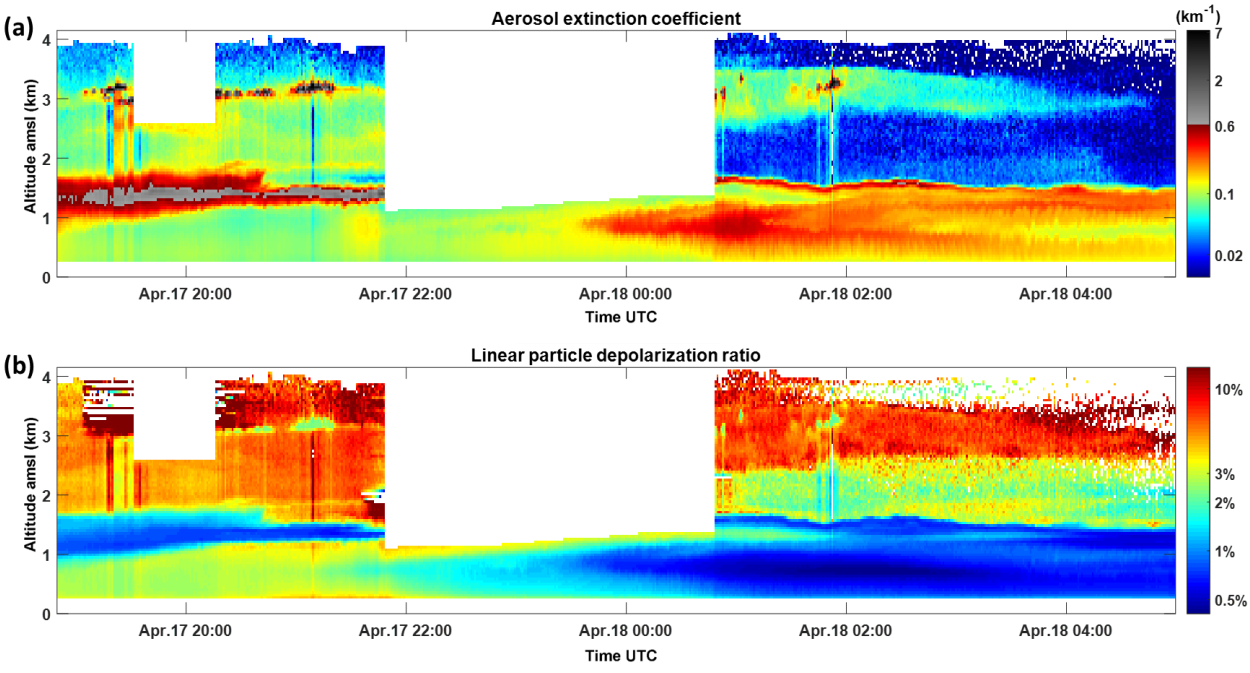

Figure 9. Time series, from 17 April 18~~50~~45 UTC to 18 April 0500 UTC, of the profiles of (a) aerosol extinction coefficient (AEC), and (b) linear particle depolarization ratio (PDR). The PDR is only considered for AEC > 0.01 km^{-1}.

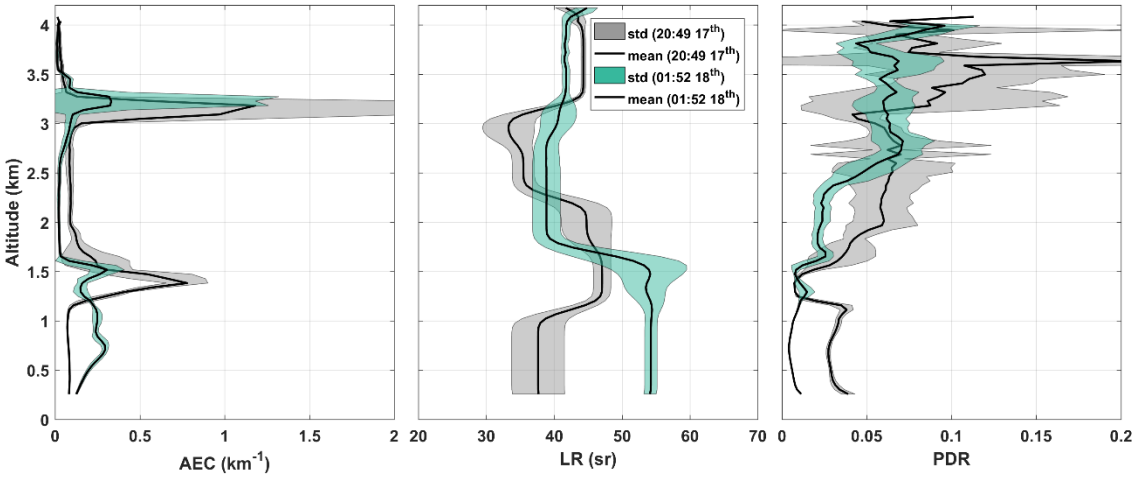

Figure 10. Examples of retrieved profiles of aerosol extinction coefficient (AEC, left), lidar ratio (LR, middle), linear particle depolarization ratio (PDR, right) for 1h lidar measurements centred on 17 April 2049 UTC and 18 April 0152 UTC. Mean values are shown by black lines and grey/green shaded areas indicate the atmospheric variability during this 1h period.

Table 2. Average optical properties (at 355 nm) for the ABL/NL (atmospheric boundary layer / nocturnal layer), the SAL (smoke aerosol layer) and the upper layer during 2 time periods (TP): TP1: 17 April, 2019–2135 UTC, TP2: 18 April, 0200–0400 UTC. The atmospheric variability during the time period is given by the standard derivation values.

Layer	ABL/NL		SAL		Upper layer	
Time period	TP1	TP2	TP1	TP2	TP1	TP2
Layer centre (km)	0.595	0.640	1.382	1.450	2.440	3.092
Thickness (km)	0.945	1.035	0.360	0.225	0.855	0.720
AEC (km^{-1})	0.086 ±0.011	0.180 ±0.015	0.444 ±0.066	0.200 ±0.054	0.090 ±0.011	0.049 ±0.013
AOD	0.08 ±0.07	0.19 ±0.02	0.17 ±0.02	0.05 ±0.01	0.08 ±0.01	0.04 ±0.01
max/min AOD	0.12 / 0.05	0.22 / 0.16	0.21 / 0.13	0.07 / 0.03	0.12 / 0.05	0.06 / 0.02
LR (sr)	41 ±9	54 ±1	46 ±3	56 ±3	40 ±5	43 ±3
PDR (%)	3.1 ±0.1	0.7 ±0.1	1.3 ±0.2	1.1 ±0.4	6.2 ±0.7	7.7 ±0.9
Possible aerosol type	Continental polluted aerosols		Fresh smoke coming from the warehouse fire		Mix of pollution and dust aerosols	

4.2 ~~Exogenous observations to confirm lidar-derived hypotheses~~Discussion

4.2.1 Comparison of the warehouse fire smoke and biomass burning smokes

The freshly emitted smoke plumes from an accidental warehouse fire was sampled. Such observations are absent in the literature, so we compared the optical properties of SAL from the warehouse fire (in Table 2**Error! Reference source not**

found.) with the ones of biomass burning smokes (Table 3). Simultaneous observations at 355 and 532 nm showed a strong wavelength dependency of the LR of aged biomass burning aerosols (Müller et al., 2007; Nicolae et al., 2013), and smaller dependency for fresh biomass burning aerosols (Nicolae et al., 2013; Pereira et al., 2014). Our measurements will be compared preferentially with other observations at 355 nm. The LR found for SAL is in the middle range of the large dispersion of 355 nm LR values (from 32 to 73 sr) found from the literatures (Table 3). Measurement of a mixed smoke and dust layer suggest that the PDR does not vary much with wavelength (Groß et al., 2011). The PDR at 355 nm of SAL (~1%) in this study is small compared to the PDR at 532 nm retrieved for smoke in the literature (2-5%, Table 3). We reported measurement of biomass burning particles with LR of ~63 and PDR of 1-4% over the Siberra region (Dieudonné et al., 2015, Table 3), using the similar lidar system.

Table 3. Optical properties found in the literature about biomass burning events and used to compare with the obtained values of the warehouse fire SAL (smoke aerosol layer) in Table 2.

Ageing	Source region	LR 355 (sr)	LR 532 (sr)	PDR 355	PDR 532	Reference
<1 day-aged	Romania	43-73	43-46	-	2–4	(Nicolae et al., 2013)
1-2 days-aged	Iberian Peninsula	52–66	49–66		3.8–5	(Pereira et al., 2014)
2-3 days-aged	Ukraine	32-48	52-54	-	2–4	(Nicolae et al., 2013)
aged	Siberia/Canada	46±13	53±11	-	<5	(Müller et al., 2007)
aged	Siberia	63±15	-	1–4	-	(Dieudonné et al., 2015)

~~4.1.1~~4.2.2 Exogenous observations to confirm lidar-derived hypotheses~~Ground-based networks~~

The total AOT and the visible Ångström exponent were extracted from the Aerosol Robotic Network (AERONET) for the sun-photometer located at Palaiseau (http://aeronet.gsfc.nasa.gov/, Figure 1~~Figure 1~~). Elevated AOT values, between 0.58 and 0.95 at 355 nm, were observed on 17 April. This is the peak value of the whole month (the monthly mean AOT is ~0.2 in cloud-free condition, corresponding to the background condition as shown by Chazette and Royer ~~(~~2017~~)~~). Nevertheless, there is only one available value (0.95) at ~1620 UTC, from 1430 UTC to the end of the day (17th April), due to the cloud cover.

Four downwind air quality stations (AS, Figure 1~~Figure 1~~a) of the AIRPARIF air quality network (http://www.airparif.asso.fr/) measured the PM_{10} concentrations at ~3 m above ground level during the warehouse fire event, as shown in Figure 1~~Figure 1~~(c). The one nearest AS1 is a traffic station, four kilometres away from the warehouse fire location. The average daytime value at AS1 on 17 April was ~60 µg m^{-3}, exceeding the information threshold for air quality; two outlying values exceed the alert threshold at around 1800 and 2000 UTC. However, there was no significant increase in PM_{10} compared to the values of the whole month. The warehouse fire mainly injected aerosols into the low free troposphere by pyro-convection, just above the ABL situated close to 1 km amsl. This kind of event appears to have negligible impact on the air quality measured at ground level. It mainly impacts the lower free troposphere, just above the ABL, as shown from lidar measurements.

~~4.1.2 Coherence between spaceborne observations and meteorological fields~~

In section 4.1, we found that lidar-derived optical parameters are quite different for aerosols in the ABL/NL before and after 17 April at 2200 UTC. It should be due to the change in air mass. In order to investigate the origins of these aerosols, back-trajectory analysis in ensemble mode was performed using the NOAA HYSPLIT (HYbrid Single-Particle Lagrangian Integrated Trajectory model, available at http://ready.arl.noaa.gov). Results show that for the first part (before 2200 UTC in Figure 9~~Figure 9~~), air mass origin is mainly from the south of France with a mix from the west of Germany; whereas for the latter one (after 2200 UTC in Figure 9~~Figure 9~~), air masses seem to be coming only from Benelux and Germany, loaded with pollution particles. Note that it was raining during the night from 16 to 17 April, and there was no rain during the day of 17 April (http://sirta.ipsl.fr/).

The origin of the upper depolarized aerosol plume, located between 1.8 and 3 km amsl (Figure 9~~Figure 9~~), was also investigated ~~using meteorological fields, as well as active and passive spaceborne remote sensing instruments~~. ~~Observations from the Cloud Aerosol Lidar with Orthogonal Polarization (CALIOP), onboard the Cloud Aerosol Lidar Pathfinder Satellite Observation (CALIPSO) (https://www.calipso.larc.nasa.gov/), were used to localize the dust aerosol plume in the free troposphere. For this, the CALIPSO Level 2 (v4.10) lidar vertical feature mask data product (Burton et al., 2013) gives precious information on the aerosol typing. The daily MODIS level 2 aerosol products (MYD04_L2 and MOD04_L2), giving the AOT at 550 nm with a spatial resolution of 10 km×10 km, was also used to highlight the temporal evolution of the dust plume transport during the observation period. Note that in the 0.4°×0.4° area around Paris, the MODIS-derived AOT is ~0.55 ± 0.09 on 17 April, matching the in situ measurements. To help understand the temporal lidar patterns and spaceborne observations,~~ ~~t~~The reanalysed products of the numerical weather prediction model ~~European Centre for Medium-range Weather Forecasts/integrated forecast system (~~ECMWF/IFS~~,~~ (http://www.ecmwf.int) are ~~also~~ used ~~with 0.30° horizontal resolution (ERA5, ECMWF Newsletter 147, page 7)~~to provide ~~.~~

~~Figure 11 shows the evolution of t~~the meteorological fields. The one at 750 hPa (~2.5 km amsl) ~~from 16 April 0000 UTC to 17 April 1800 UTC. O~~on 16 April 0000 UTC shows that~~,~~ a corridor has been created between North Africa and Western Europe, which favoured the transport of dusts, associated with a low located on the Iberian Peninsula backed by a ridge joining the Sahara to Western Europe (Figure S1 in the Supplement). The low attenuated when it moved eastward. Another more active low was enhanced near the Coruña region (Figure S1). This latter allowed a recirculation of air masses, initially loaded with dust, above the UK and then towards France. ~~Note that the arrival of the dust plume from North Africa in Western Europe is also observed on lidar measurements on 15 April 1200 UTC and this dust plume has been strengthened on 16 April 0000 UTC (not shown).~~

~~Despite the heavy cloud cover, t~~The AOT at 550 nm from daily MODIS level 2 aerosol products (MYD04_L2 and MOD04_L2)~~MODIS observations~~ also ~~(Figure 12)~~ show the transport of dusts from Morocco / Algeria to France on 16 April (Figure S2). Note that in the 0.4°×0.4° area around Paris, the MODIS-derived AOT is ~0.55 ± 0.09 on 17 April, matching the in situ measurements. These air masses moved eastward on 17 April and did not contribute directly to dust loads over the Paris area. The dust plume seen on the lidar measurements is probably related to the recirculation of air masses on 16 April. This plume is easily identified (Figure S3) as dust layers between 2 and 4 km amsl over the English Channel on the lidar vertical

feature mask data product (Level 2, v4.10, Burton et al., 2013) ~~aerosol typing products~~ derived from the CALIOP (Cloud-Aerosol Lidar with Orthogonal Polarization, https://www-calipso.larc.nasa.gov/) measurements~~, as shown in Figure 13(a). In this figure, dust layers can be observed between 2 and 4 km amsl~~. The CALIOP-derived PDR at 532 nm of this dust layer has values of the order of 30% (the related PDR at 355 nm is ~25% as proposed in Groß et al., 2015) corresponding to dust aerosols. The 6-days back trajectories (Figure S3) ~~plotted in Figure 13(b),~~ illustrate that ~~the track of~~for~~f~~ the aerosol plume examined between 1.8 and 3 km amsl~~. For air masses arriving~~ over the Paris area, a very strong recirculation can be observed on 17 April 1800 UTC. The contribution originating directly from North Africa is very weak.

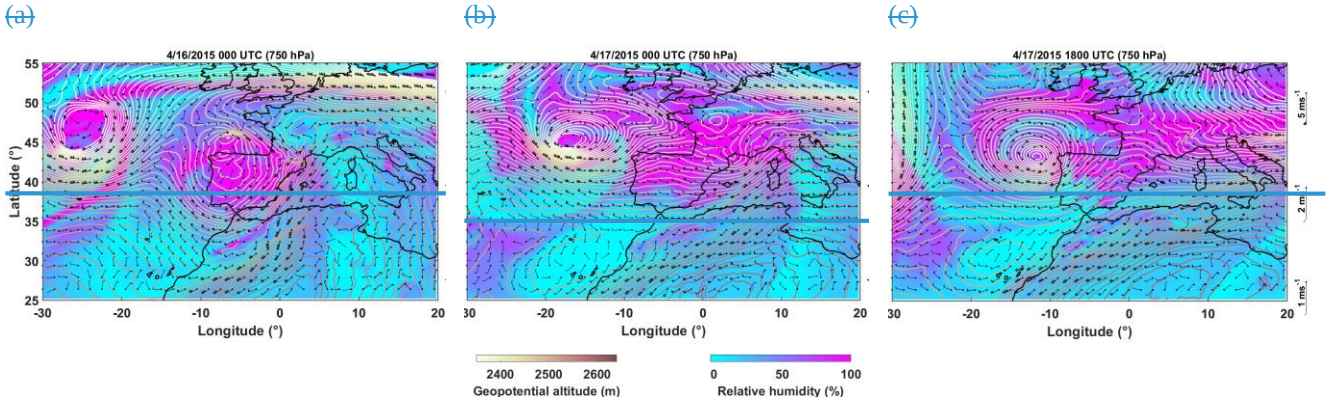

~~Figure 11. Relative humidity (%) and Geopotential altitude (m) at 750 hPa on (a) 16 April 0000 UTC, (b) 17 April 0000 UTC, and (c)17 April 1800 UTC, derived from reanalyses of numerical weather prediction model ECMWF/IFS. The wind field is also shown on each figure.~~

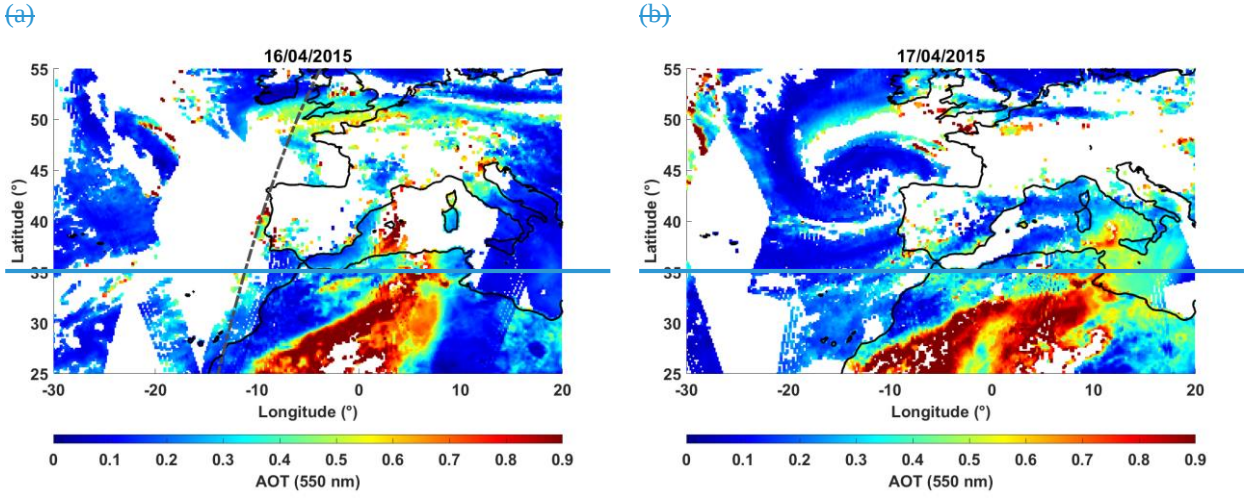

~~Figure 12. Aerosol optical thickness (AOT) at 550 nm on (a) 16 April and (b) 17 April 2015, derived from MODIS products over land and sea. The night time (~0200 UTC) ground tracks of CALIOP are given as a gray line in (a).~~

(a) (b)

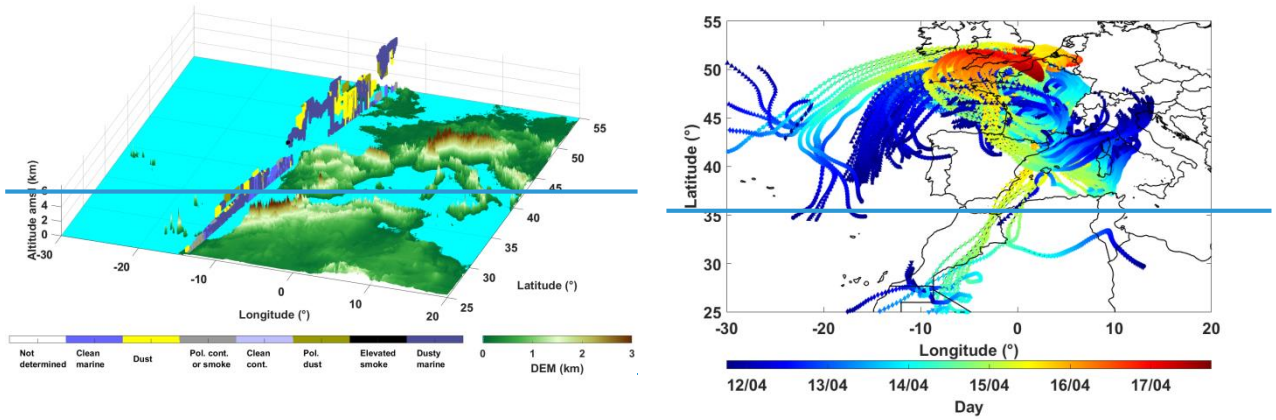

Figure 13. (a) Aerosol types on 16 April deduced from CALIOP products are plotted as a function of altitude along the ground track of the satellite. (b) Back-trajectories over 6 days, calculated using the HYSPLIT model in ensemble mode (312 back trajectories), with the temporal colour scale at the bottom. The back-trajectories endpoint is above Palaiseau, between 1.8 and 3 km amsl, following the lidar-derived vertical structure on 17 April 2015 1800 UTC.

5 Conclusions

For the first time ever, a ground based N_2-Raman lidar sampled freshly emitted smoke plumes originating from a large accidental warehouse fire that occurred on 17 April 2015. It was an exceptional event for the Paris area, but despite a strong smell throughout the region, it did not significantly exceed background aerosol levels measured by the ground-based air quality network, before it was observed by the automatic N_2-Raman lidar LAASURS located 15 km south of Paris. The lidar profiles have been inverted using a new algorithm named top-down aerosol optical thickness matching (TDAM). Such an approach allows for the retrieval of the aerosol extinction / backscatter coefficient and lidar ratio in complex cases with a highly inhomogeneous atmosphere. Furthermore, this method can be used in the event of a limited maximum range or a thick aerosol load that prevents reaching a purely molecular zone for normalization, as required by traditional methods. The uncertainties of the TDAM inversion are studied, showing good accuracy in the retrieved aerosol optical parameters: e.g. for the observed warehouse fire smoke aerosol layer, the uncertainties are 10 sr for the lidar ratio, 0.1 km^{-1} for the AEC and 0.1% for the PDR. Overall, the TDAM approach proves advantageous in heterogeneous atmospheric conditions, with a better effective vertical resolution, and less bias when there are aerosols in the free troposphere.

The optical properties of the warehouse fire smoke aerosols were characterized using this TDAM approach. This thin smoke plume, ~0.4 km wide, located at ~1.2 km amsl, has a strong AEC (~0.8 km^{-1}) and a small PDR (~1%), containing spherical, moderately absorbent aerosols. The LR of the fire smoke plume was derived as ~50 sr at 355 nm wavelength and corresponds with values previously retrieved for polluted dust aerosol or long-range transported biomass burning aerosols.

The Raman lidar system is shown once again to be a strong tool to sample aerosol layers during extreme events, which argues for the existence of lidar networks dedicated to the monitoring of air quality and airborne threats due to exceptional events that can occur in urban areas.

Acknowledgments

This work was supported by the Commissariat à l'Energie Atomique et aux énergies alternatives (CEA). The authors would like to thank the AIRPARIF network for providing ground-level aerosol data (available at http://www.airparif.asso.fr/en/telechargement/telechargement-station), the AERONET network for sunphotometer products (at https://aeronet.gsfc.nasa.gov/). The authors acknowledge the MODIS Science, Processing and Data Support Teams for producing and providing MODIS data (at https://modis.gsfc.nasa.gov/data/dataprod/), and the NASA Langley Research Center Atmospheric Sciences Data Center for the data processing and distribution of CALIPSO products (level 4.10, at https://eosweb.larc.nasa.gov/HORDERBIN/HTML_Start.cgi). The NOAA Air Resources Laboratory (ARL) is acknowledged for the provision of the HYSPLIT transport and dispersion model and READY website (http://www.ready.noaa.gov) used in this publication. ECMWF data used in this study have been obtained from the ESPRI/IPSL data server.

Author Contributions: X. Shang participated to the experiment, analysed the Raman lidar data, developed the algorithm and wrote the paper; P. Chazette conceived, managed the project, performed the experiment, developed the algorithm and participated to the paper editing; J. Totems maintained the Raman lidar, participated to the experiment and to the paper editing.
Conflicts of Interest: The authors declare no conflict of interest. The founding sponsor had no role in the design of the study; in the collection, analyses, or interpretation of data; in the writing of the manuscript, and in the decision to publish the results.

References

Ångström, A.: The parameters of atmospheric turbidity, Tellus A, 16, 64–75, doi:10.3402/tellusa.v16i1.8885, 1964.

Ansmann, A.: Ground-truth aerosol lidar observations: can the Klett solutions obtained from ground and space be equal for the same aerosol case?, Appl. Opt., 45(14), 3367, doi:10.1364/AO.45.003367, 2006.

Ansmann, A., Riebesell, M. and Weitkamp, C.: Measurement of atmospheric aerosol extinction profiles with a Raman lidar, Opt. Lett., 15(13), 746, doi:10.1364/OL.15.000746, 1990.

Ansmann, A., Wandinger, U., Riebesell, M., Weitkamp, C. and Michaelis, W.: Independent measurement of extinction and backscatter profiles in cirrus clouds by using a combined Raman elastic-backscatter lidar., Appl. Opt., 31(33), 7113, doi:10.1364/AO.31.007113, 1992.

Ansmann, A., Seifert, P., Tesche, M. and Wandinger, U.: Profiling of fine and coarse particle mass: case studies of Saharan dust and Eyjafjallajökull/Grimsvötn volcanic plumes, Atmos. Chem. Phys., 12(20), 9399–9415, doi:10.5194/acp-12-9399-

2012, 2012.

Behrendt, A., Wulfmeyer, V., Schaberl, T., Bauer, H.-S., Kiemle, C., Ehret, G., Flamant, C., Kooi, S., Ismail, S., Ferrare, R., Browell, E. V. and Whiteman, D. N.: Intercomparison of Water Vapor Data Measured with Lidar during IHOP_2002. Part II: Airborne-to-Airborne Systems, J. Atmos. Ocean. Technol., 24(1), 22–39, doi:10.1175/JTECH1925.1, 2007.

Binietoglou, I., Basart, S., Alados-Arboledas, L., Amiridis, V., Argyrouli, A., Baars, H., Baldasano, J. M., Balis, D., Belegante, L., Bravo-Aranda, J. A., Burlizzi, P., Carrasco, V., Chaikovsky, A., Comerón, A., D'Amico, G., Filioglou, M., Granados-Muñoz, M. J., Guerrero-Rascado, J. L., Ilic, L., Kokkalis, P., Maurizi, A., Mona, L., Monti, F., Muñoz-Porcar, C., Nicolae, D., Papayannis, A., Pappalardo, G., Pejanovic, G., Pereira, S. N., Perrone, M. R., Pietruczuk, A., Posyniak, M., Rocadenbosch, F., Rodríguez-Gómez, A., Sicard, M., Siomos, N., Szkop, A., Terradellas, E., Tsekeri, A., Vukovic, A., Wandinger, U. and Wagner, J.: A methodology for investigating dust model performance using synergistic EARLINET/AERONET dust concentration retrievals, Atmos. Meas. Tech., 8(9), 3577–3600, doi:10.5194/amt-8-3577-2015, 2015.

Burton, S. P., Ferrare, R. A., Vaughan, M. A., Omar, A. H., Rogers, R. R., Hostetler, C. A. and Hair, J. W.: Aerosol classification from airborne HSRL and comparisons with the CALIPSO vertical feature mask, Atmos. Meas. Tech., 6(5), 1397–1412, doi:10.5194/amt-6-1397-2013, 2013.

Chazette, P. and Royer, P.: Springtime major pollution events by aerosol over Paris Area: From a case study to a multiannual analysis, J. Geophys. Res. Atmos., 122(15), 8101–8119, doi:10.1002/2017JD026713, 2017.

Chazette, P., Pelon, J. and Mégie, G.: Determination by spaceborne backscatter lidar of the structural parameters of atmospheric scattering layers., Appl. Opt., 40(21), 3428–3440, 2001.

Chazette, P., Sanak, J. and Dulac, F.: New approach for aerosol profiling with a lidar onboard an ultralight aircraft: application to the African Monsoon Multidisciplinary Analysis., Environ. Sci. Technol., 41(24), 8335–8341, doi:10.1021/es070343y, 2007.

Chazette, P., Raut, J.-C., Dulac, F., Berthier, S., Kim, S.-W., Royer, P., Sanak, J., Loaëc, S. and Grigaut-Desbrosses, H.: Simultaneous observations of lower tropospheric continental aerosols with a ground-based, an airborne, and the spaceborne CALIOP lidar system, J. Geophys. Res., 115, doi:10.1029/2009JD012341, 2010.

Chazette, P., Dabas, A., Sanak, J., Lardier, M. and Royer, P.: French airborne lidar measurements for Eyjafjallajökull ash plume survey, Atmos. Chem. Phys., 12(15), 7059–7072, doi:10.5194/acp-12-7059-2012, 2012.

Chazette, P., Marnas, F. and Totems, J.: The mobile Water vapor Aerosol Raman LIdar and its implication in the framework of the HyMeX and ChArMEx programs: application to a dust transport process, Atmos. Meas. Tech., 7(6), 1629–1647, doi:10.5194/amt-7-1629-2014, 2014.

Chazette, P., Totems, J., Ancellet, G., Pelon, J. and Sicard, M.: Temporal consistency of lidar observations during aerosol transport events in the framework of the ChArMEx/ADRIMED campaign at Minorca in June 2013, Atmos. Chem. Phys., 16(5), 2863–2875, doi:10.5194/acp-16-2863-2016, 2016.

Collis, R. T. H. and Russel, P. B.: Laser Monitoring of the Atmosphere, edited by E. D. Hinkley, Springer Berlin Heidelberg, Berlin, Heidelberg., 1976.

Dieudonné, E., Chazette, P., Marnas, F., Totems, J. and Shang, X.: Lidar profiling of aerosol optical properties from Paris to Lake Baikal (Siberia), Atmos. Chem. Phys., 15(9), 5007–5026, doi:10.5194/acp-15-5007-2015, 2015.

Dubovik, O., Holben, B., Eck, T. F., Smirnov, A., Kaufman, Y. J., King, M. D., Tanré, D. and Slutsker, I.: Variability of Absorption and Optical Properties of Key Aerosol Types Observed in Worldwide Locations, J. Atmos. Sci., 59(3), 590–608, doi:10.1175/1520-0469(2002)059<0590:VOAAOP>2.0.CO;2, 2002.

Di Girolamo, P.: Rotational Raman Lidar measurements of atmospheric temperature in the UV, Geophys. Res. Lett., 31(1), L01106, doi:10.1029/2003GL018342, 2004.

Groß, S., Gasteiger, J., Freudenthaler, V., Wiegner, M., Geiß, A., Schladitz, A., Toledano, C., Kandler, K., Tesche, M., Ansmann, A. and Wiedensohler, A.: Characterization of the planetary boundary layer during SAMUM-2 by means of lidar measurements, Tellus B Chem. Phys. Meteorol., 63(4), 695–705, doi:10.1111/j.1600-0889.2011.00557.x, 2011.

Groß, S., Freudenthaler, V., Schepanski, K., Toledano, C., Schäfler, A., Ansmann, A. and Weinzierl, B.: Optical properties of long-range transported Saharan dust over Barbados as measured by dual-wavelength depolarization Raman lidar measurements, Atmos. Chem. Phys., 15(19), 11067–11080, doi:10.5194/acp-15-11067-2015, 2015.

Haustein, K., Pérez, C., Baldasano, J. M., Müller, D., Tesche, M., Schladitz, A., Esselborn, M., Weinzierl, B., Kandler, K. and von Hoyningen-Huene, W.: Regional dust model performance during SAMUM 2006, Geophys. Res. Lett., 36(3), n/a-n/a, doi:10.1029/2008GL036463, 2009.

Kanitz, T., Ansmann, A., Seifert, P., Engelmann, R., Kalisch, J. and Althausen, D.: Radiative effect of aerosols above the northern and southern Atlantic Ocean as determined from shipborne lidar observations, J. Geophys. Res. Atmos., 118(22), 12,556-12,565, doi:10.1002/2013JD019750, 2013.

King, L. V.: On the Complex Anisotropic Molecule in Relation to the Dispersion and Scattering of Light, Proc. Royral Soc. London, Series 1(104), 333–357 [online] Available from: http://www.researchgate.net/publication/247031191_On_the_Complex_Anisotropic_Molecule_in_Relation_to_the_Dispersion_and_Scattering_of_Light (Accessed 30 July 2014), 1923.

Klett, J. D.: Stable analytical inversion solution for processing lidar returns, Appl. Opt., 20(2), 211, doi:10.1364/AO.20.000211, 1981.

Mattis, I., Siefert, P., Müller, D., Tesche, M., Hiebsch, A., Kanitz, T., Schmidt, J., Finger, F., Wandinger, U. and Ansmann, A.: Volcanic aerosol layers observed with multiwavelength Raman lidar over central Europe in 2008–2009, J. Geophys. Res., 115, D00L04, doi:10.1029/2009JD013472, 2010.

Measures, R. M.: Laser Remote Sensing: Fundamentals and Applications, edited by J. Wiley, Krieger publishing company, Malabar, Florida, USA., 1984.

Müller, D., Ansmann, A., Mattis, I., Tesche, M., Wandinger, U., Althausen, D. and Pisani, G.: Aerosol-type-dependent lidar ratios observed with Raman lidar, J. Geophys. Res., 112(D16), D16202, doi:10.1029/2006JD008292, 2007.

Nicolae, D., Nemuc, A., Müller, D., Talianu, C., Vasilescu, J., Belegante, L. and Kolgotin, A.: Characterization of fresh and aged biomass burning events using multiwavelength Raman lidar and mass spectrometry, J. Geophys. Res. Atmos., 118(7),

2956–2965, doi:10.1002/jgrd.50324, 2013.

Nicolet, M.: On the molecular scattering in the terrestrial atmosphere : An empirical formula for its calculation in the homosphere, Planet. Space Sci., 32(11), 1467–1468, doi:10.1016/0032-0633(84)90089-8, 1984.

Pappalardo, G., Amodeo, A., Pandolfi, M., Wandinger, U., Ansmann, A., Bösenberg, J., Matthias, V., Amiridis, V., De Tomasi, F., Frioud, M., Iarlori, M., Komguem, L., Papayannis, A., Rocadenbosch, F. and Wang, X.: Aerosol lidar intercomparison in the framework of the EARLINET project 3 Raman lidar algorithm for aerosol extinction, backscatter, and lidar ratio, Appl. Opt., 43(28), 5370, doi:10.1364/AO.43.005370, 2004.

Pereira, S. N., Preißler, J., Guerrero-Rascado, J. L., Silva, A. M. and Wagner, F.: Forest fire smoke layers observed in the free troposphere over Portugal with a multiwavelength Raman lidar: optical and microphysical properties., ScientificWorldJournal., 2014, 421838, doi:10.1155/2014/421838, 2014.

Royer, P., Chazette, P., Lardier, M. and Sauvage, L.: Aerosol content survey by mini N2-Raman lidar: Application to local and long-range transport aerosols, Atmos. Environ., 45(39), 7487–7495, doi:10.1016/j.atmosenv.2010.11.001, 2011.

Sasano, Y., Browell, E. V. and Ismail, S.: Error caused by using a constant extinction/backscattering ratio in the lidar solution, Appl. Opt., 24(22), 3929, doi:10.1364/AO.24.003929, 1985.

Shang, X. and Chazette, P.: End-to-End Simulation for a Forest-Dedicated Full-Waveform Lidar Onboard a Satellite Initialized from Airborne Ultraviolet Lidar Experiments, Remote Sens., 7(5), 5222–5255, doi:10.3390/rs70505222, 2015.

Shcherbakov, V.: Regularized algorithm for Raman lidar data processing, Appl. Opt., 46(22), 4879, doi:10.1364/AO.46.004879, 2007.

Tikhonov, A. N. and Arsenin, V. Y.: Solutions of Ill-Posed Problems, Math. Comput., 32, 1320–1322, 1978.

Wang, Y., Sartelet, K. N., Bocquet, M. and Chazette, P.: Modelling and assimilation of lidar signals over Greater Paris during the MEGAPOLI summer campaign, Atmos. Chem. Phys., 14(7), 3511–3532, doi:10.5194/acp-14-3511-2014, 2014.

Weitkamp, C.: Lidar : range-resolved optical remote sensing of the atmosphere, Springer., 2005.

Whiteman, D. N.: Application of statistical methods to the determination of slope in lidar data, Appl. Opt., 38(15), 3360, doi:10.1364/AO.38.003360, 1999.

Whiteman, D. N.: Examination of the traditional Raman lidar technique I Evaluating the temperature-dependent lidar equations, Appl. Opt., 42(15), 2571, doi:10.1364/AO.42.002571, 2003.

Whiteman, D. N., Melfi, S. H. and Ferrare, R. A.: Raman lidar system for the measurement of water vapor and aerosols in the Earth's atmosphere., Appl. Opt., 31(16), 3068–3082, doi:10.1364/AO.31.003068, 1992.